Research Article

Enhanced ferro-/piezoelectric properties of tape-casting-derived Er³⁺-doped Ba₀.₈₅Ca₀.₁₅Ti₀.₉Zr₀.₁O₃ optoelectronic thick films

Jie XU, Qiling LU, Jinfeng LIN, Cong LIN, Xinghua ZHENG, Tengfei LIN, Xiao WU*

Key Laboratory of Eco-materials Advanced Technology, College of Materials Science and Engineering, Fuzhou University, Fuzhou 350108, China

Abstract: Er³⁺-doped Ba₀.₈₅Ca₀.₁₅Ti₀.₉Zr₀.₁O₃ (xEr–BCTZ, x = 0, 0.005, 0.01, 0.015) multifunctional thick films were prepared by the tape-casting method, using sol–gel-derived nano-sized powders as the matrix material. The surface morphologies, photoluminescence, and electrical properties were investigated. Dense microstructures with pure perovskite structure were obtained in the thick films. By doping an appropriate amount of Er³⁺, the samples exhibit superior up-conversion photoluminescence performance and simultaneously enhanced electrical performances. In addition, relatively higher texture fractions (with the largest value of 83.5%) were realized through introducing plate-like BaTiO₃ templates to make the thick film grow by the [001]c orientation. And the ferro-/piezoelectric properties of the thick films were further improved, showing potential in the applications of micro-optoelectronic devices.

Keywords: thick films; texture; ferroelectric; piezoelectric; photoluminescence

1 Introduction

Recently, optoelectronic multifunctional materials combining with piezo-/ferroelectric and luminescent features have attracted considerable attention by virtue of their potential electrical–optical coupling applications, such as data storage, power generation optical telecommunication, and remote sensing [1–5]. Over the past 60 years, lead-based Pb(Zr₁₋ₓTiₓ)O₃ (PZT) ceramics have governed the market of piezoelectric materials and devices. However, in face of environmental and health issues of toxic lead from PZT-based materials, people have been dedicated to searching alternative lead-free piezoelectric materials [6]. (Ba₁₋ₓCaₓ)(Ti₁₋ᵧZrᵧ)O₃, a lead-free solid solution based on barium titanate (BaTiO₃, abbreviated as BT), has achieved a breakthrough owing to the ultra-high piezoelectric coefficient (d_{33} = 620 pC/N that comparable to PZT ceramics) [7]. By constructing the morphotropic phase boundary (MPB) from a tricritical triple point of rhombohedral, tetragonal and cubic phases, the optimal composition is x = 0.15 and y = 0.1, i.e., Ba₀.₈₅Ca₀.₁₅Ti₀.₉Zr₀.₁O₃ (abbreviated as BCTZ), which also exhibits excellent ferroelectric and dielectric properties, such as relatively high remnant polarization (P_r), small electric coercive field (E_c), and large dielectric constant (ε_r).

Apart from ceramics, thick films (with the thickness ranging from 1 to 100 μm) have played vital roles since they commonly exhibit similar electrical properties

compared to ceramic bulks and can also fill the gap between ceramic counterparts and thin films. For piezo-/ferroelectric materials, thick films can withstand larger electric field to obtain greater polarization, benefitting in improving both piezoelectricity and ferroelectricity. Thus, exploring high-performance lead-free piezoelectric thick films has become imperious requirements for micro-devices such as microelectromechanical systems (MEMS) due to the drive for miniaturization, high power/sensitivity, and system integration [8–10]. Massive efforts have been made to enhance the properties of various lead-free piezoelectric thick films, for instance, bismuth sodium titanate (BNT) [11,12], potassium sodium niobate (KNN) [13–15], and BT [16–19]. However, high-performance BCTZ thick films are difficult to be fabricated by the conventional routes. Tape-casting method is usually utilized to fabricate substrate-free thick films with crystallographic texture. And tape-casting-derived textured BCTZ thick films with superior electrical performance can be achieved via a templated grain growth (TGG) process [20–22]. Plate-like BT templates with suitable aspect ratio are considered as a good candidate for preparing textured BCTZ ceramic bulks with high texture fraction (up to 98%), exhibiting significant enhancement of piezoelectric properties [20]. Therefore, the plate-like BT templates can be adopted to fabricate BCTZ-based textured thick films.

Currently, luminescent ferroelectric ceramics involving rare-earth ions (as the activator) and ferroelectrics (as the host) are widely studied to pursue the multifunctional properties [23,24]. For example, the Pr^{3+}-modified BCTZ ceramics that possess the coexistence of rhombohedral and tetragonal phases near room temperature display enhanced ferroelectric and piezoelectric responses as well as energy harvesting characteristics, exhibiting an outstanding figure of merits [25]. In addition, the Er^{3+}-doped BCTZ-based ceramics own reversible photochromism behavior, optical temperature sensing performance, and vacancy-controlled tunable opto-electronic properties [26–28]. Nevertheless, to the best of our knowledge, luminescent ferroelectric thick films have rarely been touched. If high-performance thick films can be achieved, the multifunctional applications in micro-optoelectronics will be broadened.

In the present work, Er^{3+}-doped BCTZ thick films were fabricated by tape-casting method. The relationship between performance (including piezoelectric, ferroelectric, dielectric, and up-conversion (UC) photoluminescence (PL) properties) and structure (crystal structure and microstructure) were systematically studied. Meanwhile, we obtained highly (100)-oriented Er^{3+}-doped BCTZ multifunctional thick films with improved electrical performances through the TGG process, which can promote the miniaturization of optoelectronic components and corresponding devices.

2 Experimental

2.1 Preparation of the tabular BaTiO$_3$ templates

Preparations of plate-type $BaTiO_3$ (BT) template by two-step molten salt method have been reported in the literatures [29]. To synthesize $Bi_4Ti_3O_{12}$ (BIT) precursor particles, Bi_2O_3 (99.99%, Aladdin Reagent Co. Ltd., Shanghai, China) and TiO_2 (99.99%, Aladdin Reagent Co. Ltd., Shanghai, China) were firstly mixed with molten salt (KCl, 99.5%, Aladdin Reagent Co. Ltd., Shanghai, China) and calcined at 1000 ℃ for 4 h. Then the product was washed repeatedly with hot deionized water to remove the unreacted KCl. Secondly, the obtained BIT and excessive $BaCO_3$ were mixed gently by magnetic stirring in ethyl alcohol at room temperature. And the molar ratio of BIT to $BaCO_3$ was 1:10 according to the reported applicable BT templates with appropriate size (lengths/widths around 5–12 μm) and thickness (about 0.5–1.2 μm) [20,29]. Then equal weight of NaCl (99.5%, Aladdin Reagent Co. Ltd., Shanghai, China) and KCl was added with a molar ratio of 1:1 to prepare plate-type BT particles (templates). The synthesizing temperature was 1000 ℃ and the dwell time was 3 h.

2.2 Fabrication of randomly oriented and textured *x*Er–BCTZ thick films by TGG

The 10 wt% BT textured BCTZ thick films doped with *x* mol Er^{3+} (*x*Er–BCTZ, *x* = 0 (T), 0.005 (T), 0.01 (T), and 0.015 (T), where "T" is the abbreviation of "textured") were prepared by the tape-casting method. Firstly, nanosized *x*Er–BCTZ matrix powders were synthesized by the sol–gel process using $Ba(CH_3COO)_2$ (99.99%, Aladdin Reagent Co. Ltd., Shanghai, China), $Ca(CH_3COO)_2 \cdot H_2O$ (99%, Aladdin Reagent Co. Ltd., Shanghai, China), $Ti(OC_4H_9)_4$ (99%, Aladdin Reagent Co. Ltd., Shanghai, China), $Zr(OC_3H_7)_4$ (99%, Aladdin Reagent Co. Ltd., Shanghai, China), and $Er(NO_3)_3 \cdot 5H_2O$ (99.9%, Aladdin Reagent Co. Ltd., Shanghai, China) as the raw materials. Acetate acid (99.5%, Xilong Scientific

Co., Ltd., China) and 2-methoxyethanol (99%, Sinopharm Chemical Reagent Co., Ltd., China) were used as the co-solvents and acetylacetone (99%, Sinopharm Chemical Reagent Co., Ltd., China) was acted as the chelator. Afterwards, the above chemicals were dissolved by classification, mixed and stirred to form stable *x*Er–BCTZ sols. After that, the sols were dried in oven for 12 h and ground to fine gel powders, and then calcined for 2 h at 900 ℃ in air to synthesize the *x*Er–BCTZ matrix powders. Meanwhile, ethyl alcohol (99.5%, Sinopharm Chemical Reagent Co., Ltd., China) and butanone (99%, Sinopharm Chemical Reagent Co., Ltd., China) were mixed in a volume ratio of 2:1 to obtain the solvent. And the *x*Er–BCTZ matrix powders and 10 wt% plate-type BT templates were mixed with solvent, dispersant (triethanolamine, 99.5%, Sinopharm Chemical Reagent Co., Ltd., China), binder (polyvinyl butyral, 99.5%, Sinopharm Chemical Reagent Co., Ltd., China), and plasticizer (dioctyl phthalate and polyethylene glycol with the purities of 99.5% from Sinopharm Chemical Reagent Co., Ltd., China) by stirring magnetically for 24 h to form stable slurry. Subsequently, tape-casting technique was used to align the BT templates and prepare green tapes. These tapes were diced and stacked together to desired thickness and size, and then pressed into thin plates with a thickness ~100 μm at a pressure of 150 MPa, followed by organics removal process at 800 ℃ for 2 h. Finally, the samples were sintered at 1400 ℃ in air for 4 h to obtain grain oriented (textured) *x*Er–BCTZ thick films. During the sintering stage, only grain growth of *x*Er–BCTZ occurred without reacting with the BT templates. And the preparation process belongs to the TGG method. For comparison, we also synthesized randomly oriented *x*Er–BCTZ thick films (*x*Er–BCTZ, *x* = 0 (R), 0.005 (R), 0.1 (R), 0.015 (R), where "R" stands for "randomly oriented") by the same route.

2. 3   Characterization

Purity and crystal structures of the BT templates, randomly oriented and textured *x*Er–BCTZ thick films were characterized by the X-ray diffraction (XRD) analysis (Rigaku Ultima III, Japan). Morphologies and microstructures of specimens were observed by the field-emission scanning electron microscopy (FESEM, Zeiss Supra 55, Carl Zeiss Optics co., Ltd., Germany). The morphology of pure BCTZ powders was also obtained using a transmission electron microscope (TEM) (FEI Talos F200i, USA). Archimedes drainage

method was utilized to measure the densities of the thick films. PL emission spectra were recorded by a 980 nm laser using a spectro-fluorometer (Ocean Optics USB4000, HORIBA Jobin Yvon, Paris, France). Au electrodes were sputtered on both surfaces of samples before the electrical tests. Piezoelectric coefficient d_{33} and polarization–electric field (*P–E*) loops of the thick films were measured by a quasi-static piezoelectric meter (YE2730-A, Jiangsu LIANNENG Electronic Technology Co. Ltd., Yangzhou, China) and a ferroelectric test system (TF Analyzer 2000, aixACCT, Germany), respectively. Temperature dependences of dielectric constants (ε_r) and dielectric losses (tanδ) were tested by an impedance analyzer (HP4294A, Agilent Technology (China) Co., Ltd., China).

3   Results and discussion

Figures 1(a)–1(d) show the SEM images of the *x*Er–BCTZ powders calcined at 900 ℃ for 2 h. The particle sizes of the *x*Er–BCTZ powders are fine and some agglomerations are inevitable. As shown from the XRD patterns (Fig. 1(e)), all the powders possess pure perovskite structure without obvious impurity phase. And the broadening of XRD peaks indicates
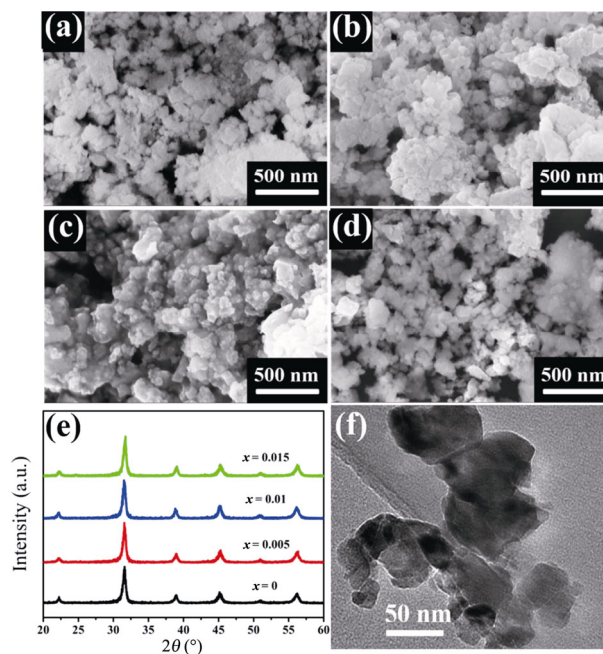

Fig. 1 (a)–(d) SEM images of the *x*Er–BCTZ powders: (a) *x* = 0, (b) *x* = 0.005, (c) *x* = 0.01, (d) *x* = 0.015. (e) XRD patterns of *x*Er–BCTZ powders calcined at 900 ℃ for 2 h. (f) TEM image of the pure BCTZ powders.

fine powders induced by the sol–gel method. To demonstrate the morphology and size distribution of calcined powders, the TEM image of the pure BCTZ powders (taking as the typical example) was observed, as shown in Fig. 1(f). It can be seen that the size distribution of the BCTZ particles is in the range of 30–60 nm. The fine powders with pure phase lay the foundation for subsequent preparation of high-quality xEr–BCTZ thick films.

Figure 2 shows the XRD pattern and SEM micrograph of the BT template. All the sharp diffraction peaks belong to tetragonal $BaTiO_3$ with the perovskite structure (JCPDS No. 75-0583), suggesting that the obtained product is well-crystallized pure phase. Besides, the (100) and (002) diffraction peaks develop obviously, indicating that the BT templates grew along the $[001]_c$ direction. The BT particles (inset of Fig. 2) show plate-type morphology with the lengths/widths of 6–12 μm and thicknesses of 0.5–1 μm. It can be predicted that those BT templates with large aspect ratio can be easily aligned and oriented during the casting process.

The XRD patterns of the randomly oriented and textured xEr–BCTZ thick films are presented in Fig. 3(a). All of them exhibit pure perovskite structure without additional diffraction peaks of impurities except for x = 0.015 (R), i.e., the randomly oriented thick film with the Er^{3+} content of 1.5 mol%. It indicates that Er^{3+} has diffused into the BCTZ lattice for all the specimens. A small amount of secondary phase ($CaTiO_3$) can be observed in x = 0.015 (R), whereas no secondary phase can be detected in x = 0.015 (T). According to the similar ionic radius, Er^{3+} (0.122 nm, coordination number CN = 12) may preferentially occupy the A-sites of Ba^{2+} (0.161 nm, CN = 12) and Ca^{2+} (0.134 nm, CN = 12) [28]. However, the incorporation of excess Er^{3+} (e.g.,

x = 0.015) will reduce the solubility limit of Ca in $BaTiO_3$, resulting in producing the $CaTiO_3$ secondary phase. For randomly oriented xEr–BCTZ thick films, the (110) diffraction peak (~32°) is the strongest while the $[001]_c$ peaks (~22°) are weak. With increasing x, the splitting of two close (002) and (200) peaks becomes more obvious (lower part of Fig. 3(b)), suggesting the enhancing stability of tetragonal BCTZ phases. Meanwhile, the (002) and (200) peaks shift towards higher angles as x increases, owing to the lattice shrinkage induced by more substitutions of smaller Er^{3+} in the A-sites of BCTZ [30]. On the other hand, for the BT templated xEr–BCTZ thick films, the intensity of $[001]_c$ peak (~22°) significantly increases accompanied by the decrease of non-$[001]_c$ peak intensities, indicating that the preferred crystallographic orientation of the templated xEr–BCTZ is along the $[001]_c$ direction. And a relatively high $[001]_c$ texture fraction of 83.5% is obtained in x = 0.01 (T), which is higher than other textured thick films (~60%). Probably due to relatively large size of BT templates (~10 μm) and relatively thin samples (with the thickness of ~100 μm), the texture fractions of the xEr–BCTZ thick films are lower than the reported textured BCTZ ceramic bulks (> 90%) [20]. It is predictable that if the thicknesses of the samples increase or the TGG process can be optimized, the texture fraction of xEr–BCTZ may further enhance. Additionally, there is no distinct deviation of the (002) and (200) peaks around 45.3° with increasing x (upper part of Fig. 3(b)), different from the randomly oriented thin films. It is known that the Ba content in the BCTZ system may influence the cationic occupation. With the introduction of BT templates in BCTZ, the ratio of Ba/Ca increases along with excess Ba^{2+}, thus Ca^{2+} can
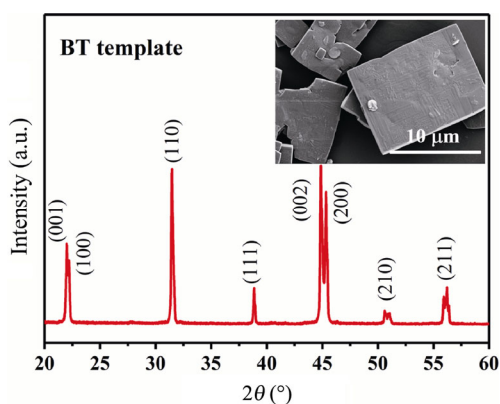

Fig. 2 XRD pattern of the BT template particles (inset is the corresponding SEM image).
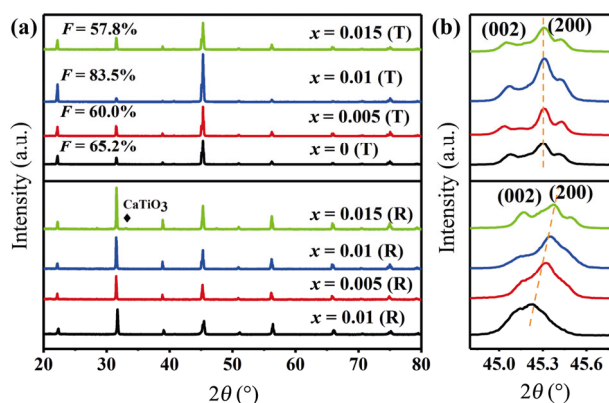

Fig. 3 (a) XRD patterns of randomly oriented and textured xEr–BCTZ thick films; (b) zoomed XRD patterns at 2θ around 45.3°.

partly shift from the Ba^{2+}-site to the Ti^{4+}-site [31]. Smaller Er^{3+} (compared with Ba^{2+} or Ca^{2+}) in the A-site and a handful of larger Ca^{2+} (compared with Ti^{4+}) in the B-site coexist in the BT templated xEr–BCTZ thick films, leading to constant positions of diffraction peaks.

Figure 4 shows the microstructures (surface and cross-section morphologies) of the xEr–BCTZ thick films. All of the specimens exhibit dense microstructures with the relative densities of > 90% (as given in Table 1). With the increase of Er^{3+} content, the average grain sizes of the randomly oriented xEr–BCTZ thick films decrease from 18.2 to 10 μm, giving the reducing factor of 45% (Table 1). As Er^{3+} occupies the A-sites by substituting for Ba^{2+} or Ca^{2+} (based on the XRD result from Fig. 3), the donor-doping behavior of Er^{3+} will induce cation vacancies, which accumulate at grain boundaries to hinder their movement during densification, resulting in inhibiting the grain growth [32]. While for the textured xEr–BCTZ thick films, the decreasing amplitude of grain size with x is relatively smaller (from 28.1 to 21.6 μm as listed in Table 1), giving the reducing factor of 23%. As aforementioned that in BT templated thick films, partly Ca^{2+} can occupy the Ti^{4+}-site, acting as the acceptor to weaken the donor effect of Er^{3+} and then partially promote the grain growth. Therefore, the textured xEr–BCTZ thick films own larger grains than their non-textured counterparts. It is interesting that there are many small and cube-shaped grains (with the mean size of ~500 nm) precipitated in the x = 0.015 (R) sample (Fig. 4(g)), corresponding to the $CaTiO_3$ secondary phase as detected by XRD (Fig. 3). The $CaTiO_3$ grains preferentially gathered at the grain boundaries and the movement of grain boundaries could be partly hindered during densification, resulting in suppression of grain growth and then smaller grains in the randomly oriented 0.015Er–BCTZ sample. In addition, the cross-section images of randomly oriented and textured xEr–BCTZ thick films are given, taking x = 0 (R) (inset of Fig. 4(a)) and x = 0 (T) (inset of Fig. 4(b)) as the examples. The thickness of each thick film is about 100 μm. Besides, the textured thick films contain more and larger pores than the non-textured ones, demonstrating that the addition of $BaTiO_3$ template is easy to bring anisotropy of the thick films and then increases the difficulty of densification. As a consequence, the relative densities of textured xEr–BCTZ thick films are lower than those of non-textured ones (Table 1). For dense textured BCTZ-based ceramic
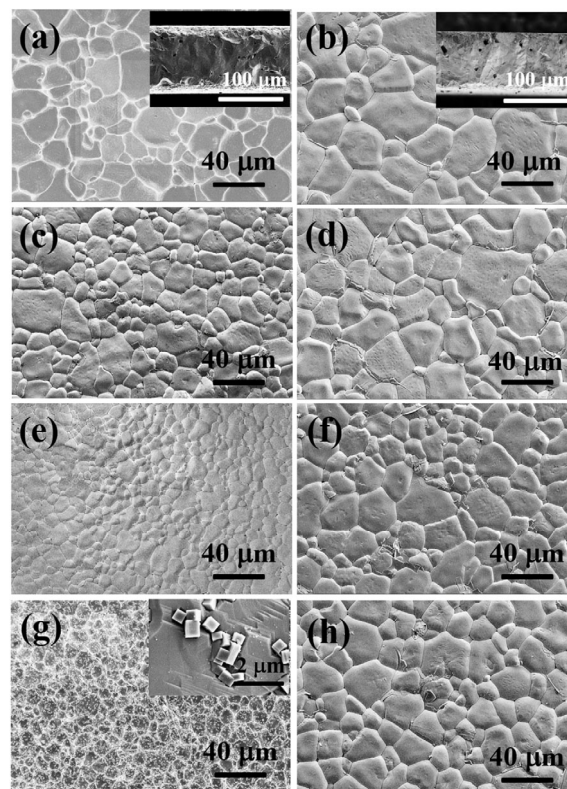

Fig. 4 SEM images of randomly oriented and textured xEr–BCTZ thick films: (a) x = 0 (R), (b) x = 0 (T), (c) x = 0.005 (R), (d) x = 0.005 (T), (e) x = 0.01 (R), (f) x = 0.01 (T), (g) x = 0.015 (R), (h) x = 0.015 (T). Insets of (a) and (b) show the corresponding cross-section images of x = 0 (R) and x = 0 (T), respectively. Inset of (g) is the partial enlarged image of x = 0.015 (R).

Table 1 Relative densities and average grain sizes of randomly oriented and textured xEr–BCTZ thick films

	x	0	0.005	0.01	0.015
Relative density (%)	Randomly oriented	95.5	96.5	97.8	97.8
	Textured	93.7	95.5	94.5	94.9
Average grain size (μm)	Randomly oriented	18.2	15.0	13.2	10.0
	Textured	28.1	25.8	22.2	21.6

bulks, polishing and thermal etching of fracture surfaces were commonly utilized to observe the specific morphology and microstructure from the view of cross-section [20]. However, the sample treatments on the fracture surface of xEr–BCTZ thick films were difficult to perform because their thicknesses are only ~100 μm. As a result, grain boundaries and morphologies of BT templates can hardly been observed in the cross-section SEM images of the xEr–BCTZ samples.

The UC PL properties of the randomly oriented and textured xEr–BCTZ thick films were investigated.

Under the excitation of 980 nm laser, room-temperature UC emission spectra of the thick films are displayed in Fig. 5. Similar to other Er^{3+}-doped BT-based materials [28,33], there are three emission bands, i.e., two strong green emission bands centered at 525 and 550 nm associated with $^2H_{11/2}/^4S_{3/2} \rightarrow {}^4I_{15/2}$, and one weak red emission band of 660 nm corresponding to $^4F_{9/2} \rightarrow {}^4I_{15/2}$ transition from Er^{3+}. The Stark splitting of the 4f energy-levels of Er^{3+} occurs under crystal field due to the interaction between Er^{3+} and the BCTZ host [34], leading to a remarkable split of three or four peaks for each emission band. All the specimens show similar PL spectral shapes. The inset of Fig. 5 shows the Er^{3+} content dependent change of normalized PL intensities for the 550 nm green emission of the xEr–BCTZ thick films. As x rises, the PL intensities of both textured and non-textured thick films tend to increase first and decrease later, giving the maximum value at $x = 0.01$. Owing to the synergistic effect of impurity phase and concentration quenching of Er^{3+}, the UC emission intensities of the thick films with $x = 0.015$ exhibit substantial decrease (compared to $x = 0.01$). In addition, the PL intensities of textured thick films are weaker than those of the non-textured ones. Two possible reasons can be responsible for the phenomenon. At a fixed Er^{3+} concentration, both the crystal symmetry and sample quality are responsible for the PL intensity. Owing to higher anisotropy around activator, the textured luminescent thick films usually exhibit stronger PL intensity than non-textured ones. Nevertheless, the PL intensities of textured xEr–BCTZ thick films are weaker than those of randomly oriented ones (the inset of Fig. 5), which can be attributed to lower relative
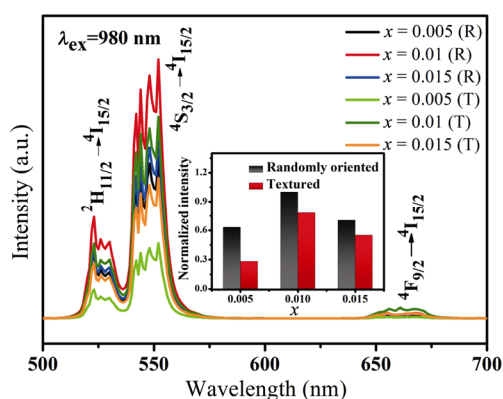
densities (Table 1) and more pores (inset of Fig. 4(b)) that are easy to scatter more light during the PL process. As a consequence, the emission intensities of textured thick films are lower.

The temperature dependences of ε_r and $\tan\delta$ of the randomly oriented and textured xEr–BCTZ thick films are given in Figs. 6(a) and 6(b), respectively. Due to local component fluctuation and charge imbalance caused by Er^{3+}-doping, the broad dielectric maxima (for both ε_r and $\tan\delta$) are observed in all the specimens, indicating the diffuse ferroelectric–paraelectric (tetragonal–cubic) transition (corresponding to the Curie temperature T_C). Only one dielectric anomaly can be observed for each specimen, manifesting that the thick films possess tetragonal phase at room temperature, which agrees well with the XRD results (Fig. 3). The T_C values of two thick films gradually decrease as the Er^{3+} concentration increases (Table 2). According to the XRD analysis (from Fig. 3), lattice contraction occurs with increasing x in randomly oriented thick films as smaller Er^{3+} substitutes for the Ba^{2+} or Ca^{2+} site. Thus, the lengths of Ti–O bonds become shorter and less energy is required to induce the phase transition from ferroelectric to paraelectric [35]. As a result, the phase transition can take place at lower temperature and T_C decreases with increasing x. On the other hand, the decrease in grain size will increase the internal stress and then reduce T_C [35]. It can be found that the change tendency of T_C is similar to that of average grain size, as compared with the data in Table 1 and Table 2. In addition, the characteristics of dense and fine-grained can enhance the dielectric properties [36,37], i.e., increasing ε_r and decreasing $\tan\delta$. Overall, the randomly oriented xEr–BCTZ thick films exhibit larger ε_r and smaller $\tan\delta$ compared with the textured counterparts. And $\tan\delta$ of the randomly oriented thick films are ~0.03 at room temperature, comparable to those of BCTZ ceramics. A modified Curie–Weiss law [38] is commonly used to characterize the degree of diffuseness:

$$1/\varepsilon_r = 1/\varepsilon_m + (T - T_m)^\gamma/C \qquad (1)$$

where C is a constant, T_m is the temperature of maximum ε_r, and ε_m is the maximum value of ε_r. The relationship between $\ln(1/\varepsilon_r - 1/\varepsilon_m)$ and $\ln(T - T_m)$ of randomly oriented and textured thick films are shown in Figs. 6(c) and 6(d), respectively. The slope obtained by fitting the curve with the least-square method is equal to γ (the diffusion coefficient). And the fitting results show that most of the γ values are about 1.6 (between 1 and 2), suggesting the relaxor-like characteristic [39].
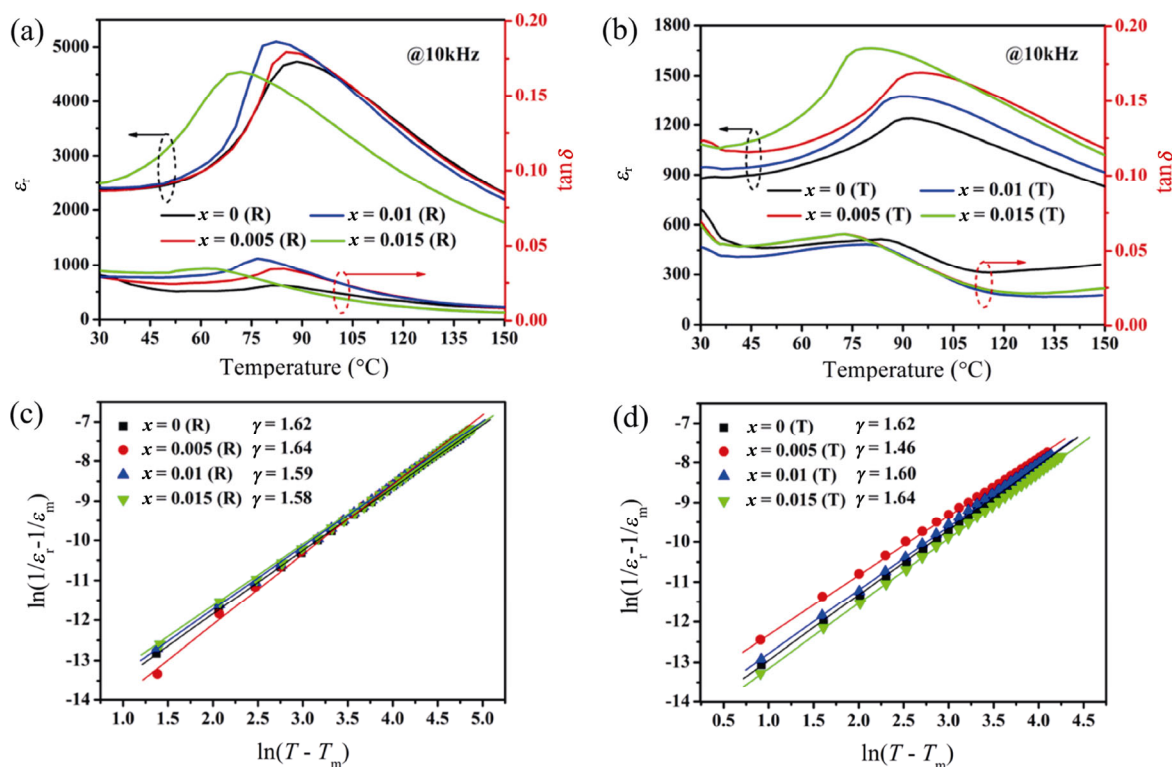

Fig. 5 Up-conversion PL emission spectra of randomly oriented and textured xEr–BCTZ thick films under the excitation of 980 nm. The inset shows the change of normalized PL intensity (at 550 nm) as a function of x.

Fig. 6 (a, b) Temperature dependences of ε_r and $\tan\delta$ of randomly oriented and textured xEr–BCTZ thick films; (c, d) $\ln(1/\varepsilon_r - 1/\varepsilon_m)$ as a function of $\ln(T - T_m)$.

Table 2 T_C of randomly oriented and textured xEr–BCTZ thick films

	x	0	0.005	0.01	0.015
T_C (℃)	Non-textured	89	86	82	71
	Textured	96	93	89	81

Figures 7(a) and 7(b) show the ferroelectric *P–E* hysteresis loops of randomly oriented and textured xEr–BCTZ thick films measured at 10 Hz under a maximum electric field of 4 kV/mm. All the specimens exhibit well-saturated and pinched hysteresis loops at room temperature. The coercive field E_c slightly increases with x (Fig. 7(c)). Since the degree of charge imbalance enhances with Er^{3+} concentration, more vacancies will produce to keep charge balance, gathering in low-energy domain walls and thus inhibiting the polarization switching to increase the E_c values [40]. Meanwhile, the remnant polarization P_r increases first and then decreases, showing that the ferroelectricity of xEr–BCTZ thick films can be improved by introducing a proper amount of Er^{3+}. As shown in Fig. 7(d), the changes of d_{33} with x display similar tendencies of P_r. The thick films with $x = 0.005$ or $x = 0.01$ (for both textured and non-textured samples) exhibit highest d_{33}.

It is known that the piezoelectric performance of thick films can be affected by density, grain size, texture fraction as well as composition. All in all, compared to randomly oriented counterparts, the textured thick films have larger P_r, smaller E_c, and higher d_{33}, implying that the motion of domain walls and polarization switching are easier to achieve. For instance, the P_r and d_{33} values of 0.005Er–BCTZ increases from 9.21 μC/cm² and 300 pC/N (randomly oriented thick film) to 12.45 μC/cm² and 343 pC/N (textured thick film), respectively (Fig. 7(d)). The optimal values of the textured 0.005Er–BCTZ thick film are $P_r = 12.45$ μC/cm², $E_c = 0.63$ kV/mm, and $d_{33} = 343$ pC/N. Probably due to comparatively lower relative densities (Table 1) and deviation from MPB by the addition of BT template during the texturing process, the enhancement of d_{33} values of the textured xEr–BCTZ thick films is not as significant as the reported pure textured BCTZ ceramics [20]. Nevertheless, the textured Er–BCTZ thick films still own larger piezoelectric coefficients compared with those pure BCTZ thick films prepared by screen printing [16,41]. Combined with UC PL feature and good di-/piezo-/ferroelectric properties, the textured Er–BCTZ thick films show potential in multifunctional optoelectronic applications.
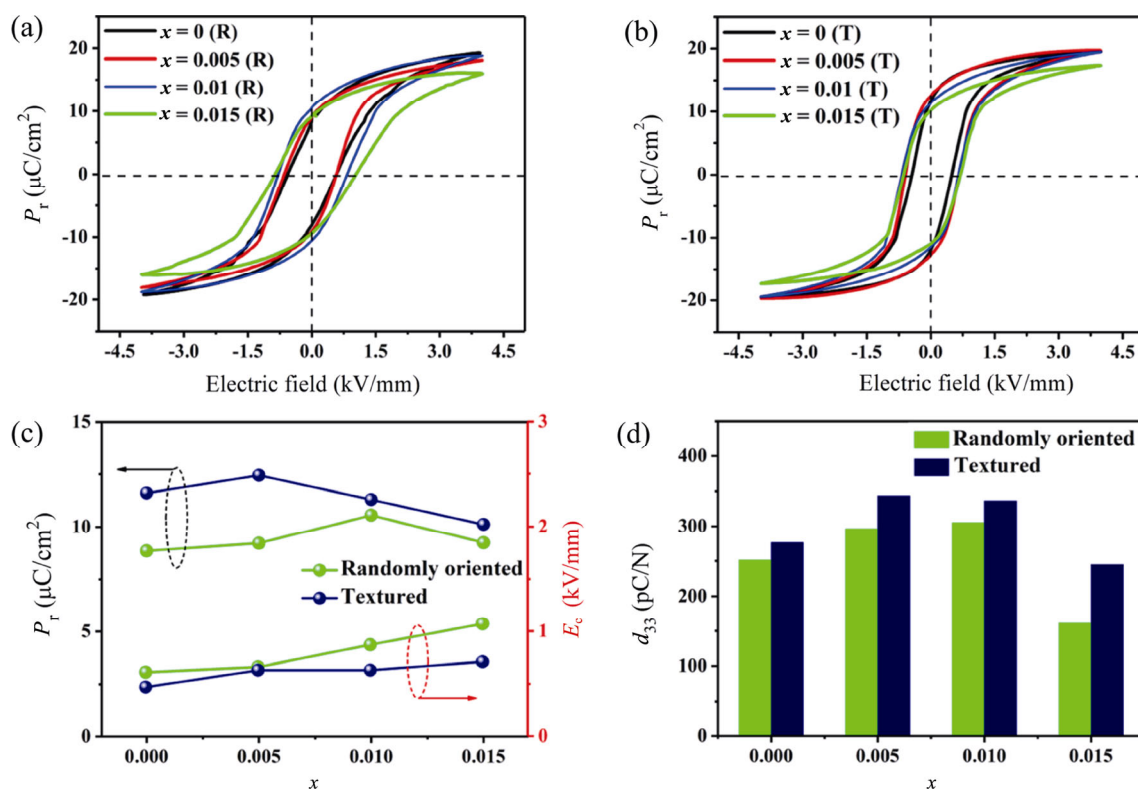
Fig. 7 *P–E* hysteresis loops of (a) randomly oriented and (b) textured *x*Er–BCTZ thick films; (c) dependence of *P*_r and *E*_c on *x*; (d) comparison of piezoelectric coefficients d_{33} of different thick films.

4   Conclusions

The randomly oriented and textured lead-free *x*Er–BCTZ thick films were synthesized by the tape-casting method. All the samples exhibit the characteristics of relatively dense (> 93%) and uniform microstructure. A high texture fraction (up to 83.5%) was realized via introducing BT templates. Appropriate doping amount of Er^{3+} can impart the PL performance, promote the compactness, and also increase d_{33}, P_r, and ε_r values. The specimens with $x = 0.01$ exhibits strongest UC emission intensity. Due to the increased light-scattering induced by larger pores, the PL intensities of textured thick films are generally lower. Compared to randomly oriented counterparts, the textured thick films exhibit larger P_r, smaller E_c, and higher d_{33} because of larger grain size and high degree orientation, giving the optimal values of $P_r = 12.45$ μC/cm^2, $E_c = 0.63$ kV/mm, and $d_{33} = 343$ pC/N. The textured thick films can be a promising candidate for optoelectronic devices.

References

[1] Kreisel J, Alexe M, Thomas PA. A photoferroelectric material is more than the sum of its parts. *Nat Mater* 2012, **11**: 260.

[2] Lu H, Bark CW, Esque de los Ojos D, *et al*. Mechanical writing of ferroelectric polarization. *Science* 2012, **336**: 59–61.

[3] Durruthy-Rodríguez MD, Gervacio-Arciniega JJ, Hernández-García M, *et al*. Photoluminescence characteristics of soft PZT 53/47 ceramic doped at A and/or B sites. *J Adv Ceram* 2018, **7**: 109–116.

[4] Zhou XT, Wu Y, Xie QX, *et al*. Magneto-electro-optical multifunctional coupling effect in lead-free BaTiO$_3$(Yb/Er)–CoFe$_2$O$_4$ ceramics. *Scripta Mater* 2020, **177**: 172–175.

[5] Lin JF, Zhou Y, Lu QL, *et al*. Reversible modulation of photoenergy in Sm-doped (K$_{0.5}$Na$_{0.5}$)NbO$_3$ transparent ceramics via photochromic behavior. *J Mater Chem A* 2019, **7**: 19374–19384.

[6] Li W, Hao JG, Li W, *et al*. Electrical properties and luminescence properties of 0.96(K$_{0.48}$Na$_{0.52}$)(Nb$_{0.95}$Sb$_{0.05}$)–0.04Bi$_{0.5}$(Na$_{0.82}$K$_{0.18}$)$_{0.5}$ZrO$_3$–*x*Sm lead-free ceramics. *J Adv Ceram* 2020, **9**: 72–82.

[7] Liu WF, Ren XB. Large piezoelectric effect in Pb-free ceramics. *Phys Rev Lett* 2009, **103**: 257602.

[8] Akedo J, Park JH, Kawakami Y. Piezoelectric thick film fabricated with aerosol deposition and its application to piezoelectric devices. *Jpn J Appl Phys* 2018, **57**: 07LA02.

[9] Torah RN, Beeby SP, Tudor MJ, *et al*. Thick-film piezoceramics and devices. *J Electroceram* 2007, **19**: 97–112.

[10] Ismail M, Wu Z, Zhang LH, *et al*. High-efficient synergy of piezocatalysis and photocatalysis in bismuth oxychloride nanomaterial for dye decomposition. *Chemosphere* 2019, **228**: 212–218.

[11] Liu YT, Ren W, Zhao JY, *et al*. Effect of sintering temperature on structural and electrical properties of lead-free BNT–BT piezoelectric thick films. *Ceram Int* 2015, **41**: S259–S264.

[12] Zhang HB, Jiang SL, Kajiyoshi K. Nonlinear dielectric properties of $(Bi_{0.5}Na_{0.5})TiO_3$-based lead-free piezoelectric thick films. *Appl Phys Lett* 2011, **98**: 072908.

[13] Han GF, Ahn CW, Ryu J, *et al*. Effect of tetragonal perovskite phase addition on the electrical properties of KNN thick films fabricated by aerosol deposition. *Mater Lett* 2011, **65**: 2762–2764.

[14] Ryu J, Choi JJ, Hahn BD, *et al*. Ferroelectric and piezoelectric properties of $0.948(K_{0.5}Na_{0.5})NbO_3–0.052LiSbO_3$ lead-free piezoelectric thick film by aerosol deposition. *Appl Phys Lett* 2008, **92**: 012905.

[15] Fu F, Shen B, Zhai JW, *et al*. Electrical properties of Li doped sodium potassium niobate thick films prepared by a tape casting process. *J Alloys Compd* 2011, **509**: 7130–7133.

[16] Feng ZY, Shi DQ, Dou SX, *et al*. Large piezoelectric effect in low-temperature-sintered lead-free $(Ba_{0.85}Ca_{0.15})(Zr_{0.1}Ti_{0.9})O_3$ thick films. *Funct Mater Lett* 2012, **5**: 1250029.

[17] Feng ZY, Luo J, Zhang W, *et al*. Enhanced piezoelectric properties of solution-modified $Ba(Zr_{0.2}Ti_{0.8})O_3–(Ba_{0.7}Ca_{0.3})TiO_3$ thick films. *J Alloys Compd* 2015, **632**: 651–654.

[18] Jian XD, Lu B, Li DD, *et al*. Large electrocaloric effect in lead-free $Ba(Zr_xTi_{1-x})O_3$ thick film ceramics. *J Alloys Compd* 2018, **742**: 165–171.

[19] Ren PR, Sun YK, Wang X, *et al*. Dielectric properties of compositionally graded $Ba_{1-x}La_xTi_{1-x/4}O_3$ thick films. *Ceram Int* 2017, **43**: 5347–5350.

[20] Liu Y, Chang Y, Li F, *et al*. Exceptionally high piezoelectric coefficient and low strain hysteresis in grain-oriented (Ba,Ca)(Ti,Zr)O₃ through integrating crystallographic texture and domain engineering. *ACS Appl Mater Inter* 2017, **9**: 29863–29871.

[21] Chang YF, Poterala SF, Yang ZP, *et al*. ⟨001⟩ textured $(K_{0.5}Na_{0.5})(Nb_{0.97}Sb_{0.03})O3$ piezoelectric ceramics with high electromechanical coupling over a broad temperature range. *Appl Phys Lett* 2009, **95**: 232905.

[22] Maurya D, Zhou Y, Yan YK, *et al*. Synthesis mechanism of grain-oriented lead-free piezoelectric $Na_{0.5}Bi_{0.5}TiO_3–BaTiO_3$ ceramics with giant piezoelectric response. *J Mater Chem C* 2013, **1**: 2102–2111.

[23] Du P, Luo LH, Li WP, *et al*. Upconversion emission in Er-doped and Er/Yb-codoped ferroelectric $Na_{0.5}Bi_{0.5}TiO_3$ and its temperature sensing application. *J Appl Phys* 2014, **116**: 014102.

[24] Hayati R, Bahrevar MA, Ganjkhanlou Y, *et al*. Electromechanical properties of Ce-doped $(Ba_{0.85}Ca_{0.15})(Zr_{0.1}Ti_{0.9})O_3$ lead-free piezoceramics. *J Adv Ceram* 2019, **8**: 186–195.

[25] Coondoo I, Panwar N, Amorín H, *et al*. Enhanced piezoelectric properties of praseodymium-modified lead-free $(Ba_{0.85}Ca_{0.15})(Ti_{0.90}Zr_{0.10})O_3$ ceramics. *J Am Ceram Soc* 2015, **98**: 3127–3135.

[26] Liu CW, Xu J, Wang QL, *et al*. Er^{3+} and $K_{0.5}Na_{0.5}NbO_3$ modified $Ba_{0.85}Ca_{0.15}Ti_{0.9}Zr_{0.1}O_3$: Novel translucent ceramics with reversible photochromism. *Ceram Int* 2019, **45**: 24348–24354.

[27] Du P, Luo LH, Li WP, *et al*. Optical temperature sensor based on upconversion emission in Er-doped ferroelectric $0.5Ba(Zr_{0.2}Ti_{0.8})O_3–0.5(Ba_{0.7}Ca_{0.3})TiO_3$ ceramic. *Appl Phys Lett* 2014, **104**: 152902.

[28] Liu CW, Wang QL, Wu X, *et al*. Boosting upconversion photoluminescence and multielectrical properties via Er-doping-modulated vacancy control in $Ba_{0.85}Ca_{0.15}Ti_{0.9}Zr_{0.1}O_3$. *ACS Omega* 2019, **4**: 11004–11013.

[29] Su S, Zuo RZ, Lv D, *et al*. Synthesis and characterization of (001) oriented $BaTiO_3$ platelets through a topochemical conversion. *Powder Technol* 2012, **217**: 11–15.

[30] Li W, Xu ZJ, Chu RQ, *et al*. Temperature stability in Dy-doped $(Ba_{0.99}Ca_{0.01})(Ti_{0.98}Zr_{0.02})O_3$ lead-free ceramics with high piezoelectric coefficient. *J Am Ceram Soc* 2011, **94**: 3181–3183.

[31] Hennings DFK, Schreinemacher H. Ca-acceptors in dielectric ceramics sintered in reducive atmospheres. *J Eur Ceram Soc* 1995, **15**: 795–800.

[32] Wu X, Kwok KW, Li FL. Upconversion fluorescence studies of sol–gel-derived Er-doped KNN ceramics. *J Alloys Compd* 2013, **580**: 88–92.

[33] Wu J, Wu Z, Mao WJ, *et al*. The photoluminescence indicating compositional changes of Er^{3+}-doped $(Ba_{1-x}Ca_x)$ $(Zr_{0.1}Ti_{0.9})O_3$ piezoelectric ceramics. *Mater Lett* 2015, **149**: 74–76.

[34] Chen L, Liang XL, Long Z, *et al*. Upconversion photoluminescence properties of Er^{3+}-doped $Ba_xSr_{1-x}TiO_3$ powders with different phase structure. *J Alloys Compd* 2012, **516**: 49–52.

[35] Ben LB, Sinclair DC. Anomalous Curie temperature behavior of A-site Gd-doped $BaTiO_3$ ceramics: The influence of strain. *Appl Phys Lett* 2011, **98**: 092907.

[36] Buessem WR, Cross LE, Goswami AK. Phenomenological theory of high permittivity in fine-grained Barium titanate. *J Am Ceram Soc* 1966, **49**: 33–36.

[37] Awan MQ, Ahmad J, Sun QB, *et al*. Structure, dielectric and ferroelectric properties of lead-free (Ba,Ca)(Ti,Zr)O₃–xBiErO₃ piezoelectric ceramics. *Ceram Int* 2018, **44**:

6872–6877.

[38] Uchino K, Nomura S. Critical exponents of the dielectric constants in diffused-phase-transition crystals. *Ferroelectrics* 1982, **44**: 55–61.

[39] Zhang DH, Zhang YL, Yang SH. Microstructure and electrical properties of tantalum doped $(Ba_{0.85}Ca_{0.15})(Zr_{0.10}Ti_{0.90})O_3$ ceramics. *J Mater Sci: Mater Electron* 2015, **26**: 909–915.

[40] Noguchi Y, Miwa I, Goshima Y, *et al*. Defect control for large remanent polarization in bismuth titanate ferroelectrics-doping effect of higher-valent cations. *Jpn J Appl Phys* 2000, **39**: L1259–L1262.

[41] Bai WF, Shen B, Fu F, *et al*. Dielectric, ferroelectric, and piezoelectric properties of textured BZT–BCT lead-free thick film by screen printing. *Mater Lett* 2012, **83**: 20–22.